PAPER

Check for updates

A tube-like Pd@coordination polymer with enhanced solar light harvesting for boosting photocatalytic H$_2$ production in a wide pH range and seawater†

Jieling Li,‡ Shihao Sun,‡ Ningshuang Gao, Hua Li, Kun Liang,* Jun Hai, Suisui He, Xijiao Mu* and Baodui Wang [ORCID] *

Coordination polymers (CPs) have emerged as promising candidates for photocatalytic H$_2$ production owing to their structural tailorability and functional diversity. However, the development of CPs with high energy transfer efficiency for highly efficient photocatalytic H$_2$ production in a wide pH range still faces many challenges. Here we constructed a novel tube-like Pd(II) coordination polymer with well-distributed Pd nanoparticles (denoted as Pd/Pd(II)CPs) based on the coordination assembly of rhodamine 6G and Pd(II) ions and further photo-reduction under visible light irradiation. Both the Br$^-$ ion and double solvent play a key role in forming the hollow superstructures. The resulting tube-like Pd/Pd(II)CPs exhibit high stability in aqueous solution with the pH range from 3 to 14 due to the high Gibbs free energies of protonation and deprotonation, which provides the feasibility of photocatalytic hydrogen generation in a wide pH range. Electromagnetic field calculations showed that the tube-like Pd/Pd(II)CPs have a good confinement effect on light. Therefore, the H$_2$ evolution rate could reach 112.3 mmol h^{-1} g^{-1} at pH 13 under visible light irradiation, which is far superior to those of reported coordination polymer-based photocatalysts. Moreover, such Pd/Pd(II)CPs could also reach a H$_2$ production rate of 37.8 mmol h^{-1} g^{-1} in seawater under visible light with low optical density (40 mW cm^{-2}) close to morning or cloudy sunlight. The above unique characteristics make the Pd/Pd(II)CPs possess great potential for practical applications.

1. Introduction

Replacing fossil energy with clean energy is an effective measure to solve the problems of environmental pollution and energy crisis. In recent years, renewable clean energy and related technologies have received increasing attention.[1,2] Hydrogen is widely regarded as a promising energy source due to its high energy density and no environmental pollution.[3] Since the groundbreaking report by Fujishima and Honda in 1972,[4] photocatalytic hydrogen evolution from water has been considered a promising method for using solar energy to obtain clean and sustainable energy.[5] A large number of semiconductors, such as TiO$_2$,[6] g-C$_3$N$_4$,[7] and transition metal sulfides,[8,9] have been widely developed as photocatalysts for hydrogen evolution. However, the H$_2$-production activities are unsatisfactory, and unfavorable thermodynamics, slow kinetics,

dissolved oxygen, reverse reactions, and side reactions make the overall photocatalytic cracking of water very difficult.[10] In addition, most of these reported materials so far have carried out photocatalytic hydrogen evolution in a narrower pH range, scarce pure water, and high light density, and their conversion efficiency is still very low, which limits their practical applications.[11] Notably, the majority of the water resources on the earth come from the ocean, so it is of enormous economic significance to produce hydrogen directly from seawater.[12]

Coordination polymer (CP)-based superstructures[13] with structural tailorability and functional diversity have received considerable attention and interest for application in photocatalytic systems. Especially, CPs constructed from metal-containing nodes and fluorescent dye group-based ligands through a strong coordinate bond have been developed as ideal photocatalysts for photo-harvesting[14,15] and the photocatalytic splitting of water[16] due to their inherent excellent optical absorption and emission as well as funnel electron transport and energy transfer.[17] Some studies have found that one-dimensional (1D) structure photocatalysts can realize shorter transfer distances of charge carriers, thereby improving the separation efficiency of photoexcited electrons and holes.[18]

State Key Laboratory of Applied Organic Chemistry, Key Laboratory of Nonferrous Metal Chemistry and Resources Utilization of Gansu Province, Lanzhou University, Gansu, Lanzhou 730000, China. E-mail: haij@lzu.edu.cn; wangbd@lzu.edu.cn

† Electronic supplementary information (ESI) available: Experimental details, synthesis and characterization. See DOI: https://doi.org/10.1039/d3na00252g

‡ These authors contributed equally to this work.

Meanwhile, hollow-structure photocatalysts have several unique advantages including a shorter transfer distance, high light-harvesting efficiency, and more reaction sites.[19–23] However, only a few kinds of CP hollow superstructures were synthesized.[24] In particular, the photocatalytic efficiency of these CP systems is still very low, and the photocatalytic hydrogen evolution reaction can only work in a narrow pH range and scarce pure water,[25,26] which limited their practical applications. Thus, it remains highly desirable to synthesize new CP hollow superstructures with high energy transfer efficiency for highly efficient photocatalytic H_2 production in a wide pH range.

In the present work, a double-solvent strategy was used to synthesize template-free Pd(II) coordination polymer tubes with well-distributed Pd nanoparticles based on coordination assembly and coordination-induced fusion of rhodamine 6G (Rh6G) and Pd(II) ions. The resulting Pd/Pd(II)Rh6GCPs (denoted as Pd/Pd(II)CPs) exhibit a wider absorption window in the visible region. Importantly, in such superstructures, the Gibbs free energies of the protonation and deprotonation are greater than 10 kcal mol^{-1}, making protonation or deprotonation difficult to occur at room temperature. Therefore, Pd/Pd(II)CP superstructures possessed high stability in an aqueous solution with a pH range from 3 to 14, which provided the feasibility of photocatalytic hydrogen generation in a wide pH range. In such hollow superstructures, the Pd(II)CPs and the Pd nanoparticles (NPs) act as the photoactive center and catalytic center, respectively, and the hollow structure provides a cavity for efficient solar light harvesting. In the photocatalytic process, the separation of photogenerated carriers is often the decisive step of the reaction. In our system, photoexcited electrons transfer rapidly from eosin Y (EY) to Pd(II)CPs at the interface, and electrons can be rapidly captured and utilized by *in situ* Pd NPs, which significantly improves the electron–hole separation efficiency. An amazing H_2 production rate of 112.3 mmol h^{-1} g^{-1} was obtained. To our knowledge, these are the first reported CP superstructures with the highest H_2 production rate in a wide pH range.

2. Experimental section

2.1. Materials

All of the chemicals were purchased from commercial sources without further treatment. PdCl$_2$ (Pd > 47.8%) was obtained from Beijing HWRK Chem Co. Rhodamine (for biological staining, dye content, ≥90%) and NaBr was from Tianjin Kaitong Chemical Reagent Co. All chemicals were used without further purification. Ultra-pure water was used in the study. Deionized water (DI-water) was used throughout the experiments. The seawater involved in the experiment was real seawater (South China seawater, taken from Hainan Province).

2.2. Synthesis of Pd(II)CPs and Pd/Pd(II)CPs

For the preparation of Pd(II)CPs, 9 mL ethanol and 7 mL water were added into the reaction vessel, and then 3 mL PdCl$_2$ (1.0 mmol L^{-1}), 3 mL Rh6G (3.0 mmol L^{-1}) and 10 mg NaBr

were added to the above reaction vessel. The reaction mixture was illuminated under visible light (420 nm < λ < 780 nm filter) for 1 h. The formed productions were collected by centrifugation with 8000 rpm and washed several times with water until the supernatant had no color. The above reaction was extended for 1 h to obtain Pd/Pd(II)CPs.

2.3. Synthesis of Pd/Pd(II)CP rods (denoted as Pd/Pd(II)CPRs)

Water (4 mL) was placed in the reaction vessel with PdCl$_2$ (3 mL, 1.0 mmol L^{-1}), Rh6G (3 mL, 3.0 mmol L^{-1}) and NaBr (10 mg). The reaction mixture was illuminated under visible light (420 nm < λ < 780 nm filter) for 2 h. The formed productions were collected by centrifugation with 8000 rpm and washed several times with water until the supernatant had no color.

2.4. Photocatalytic activity evaluation

Typically, 5 to 20 mg EY mixed with a 1 mg Pd/Pd(II)CP sample was dispersed in a mixed solution of 12 mL of deionized water and 1 mL of triethanolamine (TEOA). The above system was sealed in a gas-closed system with a top irradiation quartz cell of 50 mL at 25 °C, and the air in the pool was discharged after 20 min of nitrogen purge. After that, a Xe lamp equipped with a 400–780 nm filter was used for irradiation. The light intensity was controlled to 500 mW by using an optical density instrument, and the temperature was controlled at 25 °C during illumination. The amount of hydrogen generated from photocatalytic water splitting at different times was measured by using a Shimadzu GC-2014C gas chromatograph equipped with a TCD detector and a capillary column using high purity argon gas as a carrier gas.

The hydrogen production performance under different light intensities was studied by adjusting the distance between the reactor and the light source, and the light intensities were measured using a power meter (Newport 843-R). For the control experiment, the experimental conditions were the same as the above steps, except that 20 mg eosin was used each time and mixed with 1 mg PdCPs and 1 mg Pd/Pd(II)CPRs, respectively. For light-intensity dependence study, the light intensity was adjusted by making the corresponding changes in the distance between the reactor and the light source, and the exact light intensity was measured with a power meter (Newport 843-R). For the hydrogen production performance of water with different pH values and seawater, the dosage of the corresponding substances and the experimental process are the same as the above steps, except that distilled water is changed into water with different pH values and seawater.

2.5. Chemical stability test

The aqueous solutions of pH 3, 5, 7, 9, 11, 13 and 14 were prepared, and then Pd/Pd(II)CPs were soaked in each solution for 12 h. After that, all of the samples were centrifuged, washed three times with water, and dried in an oven for further PXRD measurement.

2.6. Photocurrent measurements

The Pd/Pd(II)CP sample (2 mg) was added to a solution of 10 μL of 5 wt% Nafion and 1.5 mL of water. After that 50 μL of the suspension solution was added dropwise onto ITO and dried at room temperature to prepare the working electrode. Photocurrent measurements were performed on a CHI 760E electrochemical workstation (Chenhua Instrument, Shanghai, People's Republic of China) in a standard three-electrode system with T-Pd-Rh6G-coated ITO as the working electrode, a Pt plate as the counter electrode, and Ag/AgCl as a reference electrode. A 300 W Xe lamp with a UV cutoff filter ($\lambda > 420$ nm) was used as the light source. The photocurrent was measured under open circuit potential in 0.5 M Na_2SO_4 electrolyte solution.

2.7. Mott–Schottky plot measurements

The electrochemical performance was determined using an electrochemical workstation (Metrohm Autolab, PGSTAT302) in a standard three-electrode system with Pd/Pd(II)CP coated ITO as the working electrode, a Pt plate as the counter electrode, and Ag/AgCl as a reference electrode at frequencies of 500, 1000, and 1500 Hz, respectively. A 0.5 M Na_2SO_4 solution was used as the electrolyte.

2.8. Electrochemical impedance spectroscopy measurements

The electrochemical performance was determined using an electrochemical workstation (Metrohm Autolab, PGSTAT302) in a standard three-electrode system with Pd/Pd(II)CP coated ITO as the working electrode, a Pt plate as the counter electrode, and Ag/AgCl as a reference electrode. The EIS plots were recorded at open circuit potential from 100 kHz to 0.1 Hz with an AC voltage of 5 mV in a 2.5 mM Fe^{2+}/Fe^{3+} electrolyte.

2.9. Photocatalytic reactions

The photocatalytic reactions were performed under visible light ($\lambda > 420$ nm) irradiation from a 300 W Xe lamp combined with a UV-cut-off filter (L42, Hoya Co, Japan). The hydrogen was analyzed using a gas chromatograph equipped with a TCD detector. The apparent quantum yield (AQY) of hydrogen production was measured using various band-pass optical filters. The numbers of incident photons were measured using a radiant power energy meter (Newport 843-R). The AQY was calculated by using the following equation:

$$AQY \ (\%) = \frac{number \ of \ evolved \ H \ molecules \times 2}{number \ of \ incident \ photons} \times 100\%$$

3. Results and discussion

3.1. Synthesis and characterization of Pd(II)CPs and Pd/Pd(II)CPs

The procedures for the preparation of the Pd(II)CPs and Pd/Pd(II)CPs are described in Fig. 1a. To determine the structure of

CPs, we used the meta-dynamic genetic algorithm (MTD-GC) to perform a conformation search for different ratios of Pd^{2+} ions and Rh6G molecules in different proportions. As shown in Fig. 1b and S1,† the intermolecular interactions were almost identical for different ratios of metal ions and ligands. Fig. 1b shows that each Pd^{2+} ion (the larger black sphere) coordinated with the alkoxy oxygen in the ester group and the C-9 in the pyran ring, and the formed coordination polymers were arranged in a chain-like structure in space. To further confirm the plausibility of the structure, the Pd^{2+} coordination with the alkoxy oxygen and the C-9 was proved by solid-state ^{13}C cross-polarization magic-angle spinning (CP/MAS) NMR spectroscopy. As shown in Fig. 1c, the ^{13}C NMR signal of C-9, C-20, C-21, and C-22 in Rh6G was at 114.6, 166.7, 59.4, and 13.6 ppm, respectively, while the corresponding three carbons were shifted to 113.2, 165.7, 62.2, and 16.2 ppm, respectively, in Pd(II) CPs[26] (Table S1†). This result identified the Pd^{2+} coordination with the alkoxy oxygen and the C-9. In addition, the calculated ^{13}C NMR spectrum also further confirmed the above coordination (Fig. S2†).

FT-IR spectra showed that the alkoxy (O–C) stretching vibration shifted from 1088 cm^{-1} in Rh6G to 1079 cm^{-1} in Pd(II) CPs (Fig. S3†).[27] In addition, compared with free Rh6G, a new absorption band at 505 cm^{-1} indicated the formation of a Pd–O bond. We also calculated the FT-IR spectra of Rh6G and Pd(II) CPs using density functional theory (DFT) and diffusion basis functions. Fig. S4† shows that the infrared absorption peak of Rh6G at 1036 cm^{-1} is blue-shifted to 1029 cm^{-1} in Pd(II)CPs, and the degree of blue-shift is consistent with the experiment. Moreover, as in the experimental spectrum, the Pd(II)CPs showed new absorption peaks at 455 cm^{-1} (Fig. S4, Table S2†). The calculated ^{13}C NMR spectrum and FT-IR spectra are in good agreement with the experimentally measured spectra,[28,29] which further shows that the structure of the complex searched by the MTD-GC method is similar to the actual structure.

To generate the tube-like CP superstructures, Rh6G and palladium ions were used as precursors and Br^- was used as the structure-directing agent. Scanning electron microscopy (SEM) images (Fig. 2a and b) and transmission electron microscopy (TEM) images (Fig. S5†) showed that both Pd(II)CPs and Pd/Pd(II)CPs possessed a hollow tubular structure with 2–3 μm width, 40–50 μm length and 0.3 μm thickness. Compared with Pd(II)CPs, the high resolution TEM (HRTEM) images of Pd/Pd(II) CPs showed that Pd NPs with an average size of 2.45 nm were evenly embedded on the tube (Fig. 2c and S6†), indicating that some Pd^{2+} ions were converted to Pd NPs by photoreduction. The lattice spacing of 0.22 nm was attributed to the (111) planes of Pd (Fig. 2d).[30,31] The HAADF-STEM images and elemental mappings (Fig. 2e) of Pd/Pd(II)CPs showed that Pd, O, N, and Br were uniformly distributed throughout the whole tube, which was further confirmed by EDS analysis (Fig. S7†). The Pd loading amounts of Pd(II)CPs and Pd/Pd(II)CPs were 12.3 and 18.1 wt%, respectively, based on inductively coupled plasma atomic emission spectroscopy analyses.

The formation process of Pd(II)CP superstructures was tracked by SEM, and the reaction conditions and corresponding morphology of superstructures are concluded in Fig. 2f. As
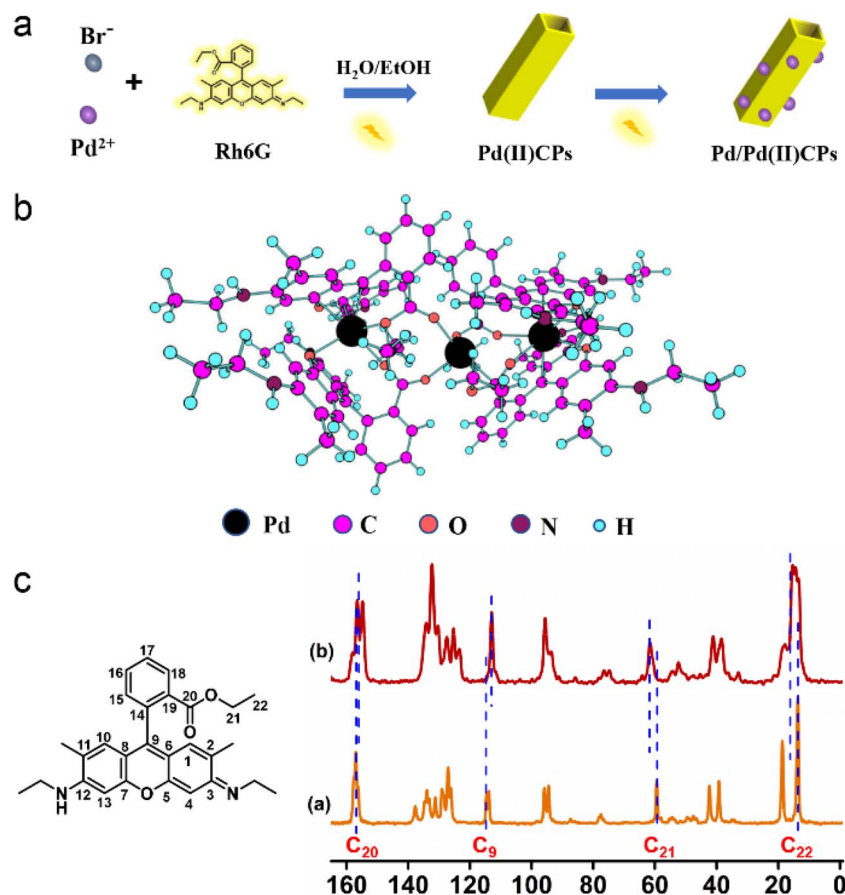
Fig. 1 (a) Schematic illustration of the preparation of Pd(II)CPs and Pd/Pd(II)CPs. (b) The structure of Pd(II)CPs searched by the MTD–GC method. (c) Partial ^{13}C MAS NMR spectra (600 MHz): (a) Rh6G; (b) Pd(II)CPs.

shown in Fig. S8a,† the morphology changed from the irregular sheet-like structure in the first five min to tubular structures one hour later. Upon further prolonging the reaction time to 3 h, no apparent changes in the size and structure of the tube were observed. The observations indicate that coordination interactions between the Rh6G and the Pd^{2+} ions contribute to the transformation from a sheet-like structure to a hollow tube. Therefore, we can conclude that these superstructures may be generated by a unique metal-coordination-induced fusion process, which is similar to previously reported hollow superstructures.[32] In addition, solvent-dependent experiments showed that no tubular structures were observed in the water medium alone, but only rod-like structures were obtained (Fig. S8b†). In addition, no fixed structure was formed in ethanol. Time-dependent experiments showed that the tube structure was not observed in the reaction system without Br^- ions (Fig. S8c†). The above observations indicated that Br^- ions and dual solvent of water and ethanol played key roles in the formation of tubular structures. Here, Br^- ions change the order of the surface energy of different faces due to their strong electronegativity, allowing the formation of tubular structures,[33] and the good solubility of Rh6G in ethanol helps to form a hollow tube in coordination-induced assembly of Rh6G and the Pd^{2+} ions.[32]

As shown in Fig. 3a, the powder X-ray diffraction (XRD) profile indicated that both Pd(II)CPs and Pd/Pd(II)CPs displayed narrow diffraction peaks, suggesting the high crystallinity of the resultant products. Compared with Pd(II)CPs, the main diffraction peak appearing at 40.4° in Pd/Pd(II)CPs further indicated the presence of Pd NPs.[34] The X-ray photoelectron spectroscopy (XPS) spectrum of Pd(II)CPs and Pd/Pd(II)CPs is shown in Fig. S9.† The results showed that besides C, N, O, and Br peaks, peaks assignable to the $3d_{5/2}$ and $3d_{3/2}$ levels of Pd^{2+} species were observed in both Pd(II)CPs and Pd/Pd(II)CPs (Fig. 3b and S10†). Compared with Pd(II)CPs, peaks assignable to the $3d_{5/2}$ and $3d_{3/2}$ levels of Pd^0 species at 334.61 and 339.83 eV were observed in Pd/Pd(II)CPs, indicating the presence of Pd NPs in Pd/Pd(II)CPs.[29] Moreover, compared with the O 1s peaks of free Rh6G, the O 1s peaks of Pd/Pd(II)CPs were shifted and a new peak appeared, further indicating that Pd^{2+} coordinated with the O atom (Fig. S11†).

UV/Vis diffuse reflection (DR) spectroscopy showed that the absorption edge of Pd/Pd(II)CPs extended to about 750 nm, while Rh6G only showed an abrupt absorption edge at about 520 nm (Fig. 3c). The broadened absorption peak was due to the existence of the d–d transition of the Pd^{2+} ions and ligand-to-metal charge transfer in the Pd/Pd(II)CPs.[35] The optical band gap was estimated to be 2.08 eV using the Kubelka–Munk
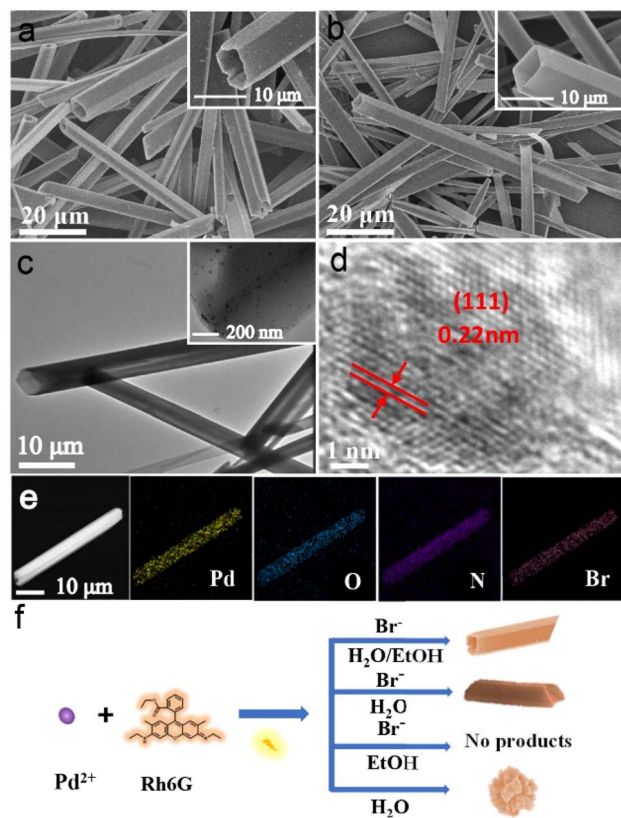
Fig. 2 (a and b) SEM image of Pd(II)CPs and Pd/Pd(II)CPs. (c) TEM image of Pd/Pd(II)CPs (inset: HRTEM image). (d) HRTEM image of Pd/Pd(II)CPs. (e) HAADF-STEM image and EDS elemental mappings of Pd, O, N, and Br. (f) Schematic diagram of the formation of Pd/Pd(II)CPs under different reaction conditions.
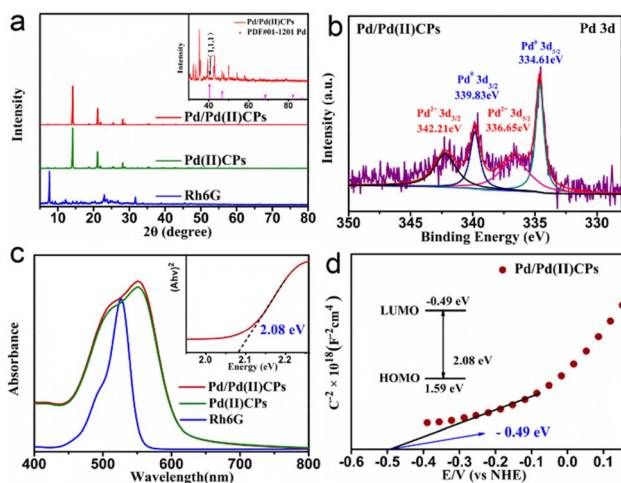

Fig. 3 Structural characterization and optical properties of Pd(II)CPs and Pd/Pd(II)CPs. (a) Powder XRD patterns of Pd(II)CPs and Pd/Pd(II)CPs. (b) Pd 3d XPS spectra of Pd/Pd(II)CPs. (c) UV/Vis DR spectra of Pd(II)CPs and Pd/Pd(II)CPs, and the inset shows the determination of the optical band gap. (d) Mott–Schottky plots for Pd/Pd(II)CPs.

equation (inset of Fig. 3c).[36] In addition, Mott–Schottky analysis was performed to accurately determine the band energy levels of Pd/Pd(II)CPs. The lowest flat potential was −0.49 eV by

extrapolating the intercept on the potential axis. Then the highest flat potential was derived from the band gap to be +1.59 eV (Fig. 3d).

3.2. Photocatalytic hydrogen evolution experiments

Here, we introduced alcohol-soluble Eosin Y (EY) as a photosensitizer into the photocatalytic system to be combined with Pd/Pd(II)CPs for light capturing because the absorption of Pd/Pd(II)CPs matched with the emission of EY (Fig. S12†). Fig. 4a shows that the H_2 evolution rate of Pd/Pd(II)CPs could reach up to 112.3 mmol h^{-1} g^{-1} with triethanolamine (TEOA) as the hole scavenger (H_2O/TEOA, 12 : 1 v/v) in pure water at pH 13, which is the highest among the reported coordination polymer photocatalysts for generating H_2 from water so far (Table S3†). There is no hydrogen production effect when EY is not added, indicating that EY is a significant electron donor in this system. As a control experiment, Pd/Pd(II)Rh6GCP rods (denoted as Pd/Pd(II)CPRs) were used to test the photocatalytic hydrogen evolution reaction under the same conditions. As shown in Fig. S13,† the H_2 evolution rate of Pd/Pd(II)CPRs (86.1 mmol h^{-1} g^{-1}) was lower than that of Pd/Pd(II)CPs. The above results indicate that the hollow structure is beneficial for enhancing the activity of photocatalytic H_2 evolution. The reason is that the hollow structure provides a cavity for efficient solar light harvesting on Pd/Pd(II)CPs.[37,38] To illustrate the propagation process of light in microtubes, we use the finite difference time domain (FDTD) algorithm for electromagnetic field calculations. Among them, the incident wave uses a Gaussian beam with a power of 1 W and a grid size of 0.1 nm. Unlike the conventional light propagation length with a field strength of 1/e as the endpoint, the electric field strength decays to 0 as the endpoint of the propagation length in a propagation length calculation. The refractive index of CPs is calculated by DFT, and the liquid environments are pure water and seawater, respectively. As shown in Fig. 4b, when the incident light is parallel to the microtube, the propagation depth of the light can reach 90 μm. However, when the incident light is perpendicular to the tube, the propagation depth of the light is only 10 μm. In addition, the electric field intensity distribution in the microtube further shows that the tubular structure has a good confinement effect on the light, which makes the light travel a long distance in the microtube (Fig. 4c and d). In this way, more light is involved in the photocatalytic reaction, which ultimately improves photocatalytic efficiency.

As we all know, the pH value of the solution has a great influence on the photocatalytic activity of the catalysts.[39] The existing state of dye and TEOA could be regulated by the pH value in the photocatalytic system of dye sensitization, which affects the evolution rate of H_2.[40] The powder XRD pattern proved that the formed Pd/Pd(II)CPs displayed high stability in aqueous solutions over a broad pH range from 3 to 14 (Fig. 4e), which was rarely observed in other CPs.[41] Fig. 4f shows that the H_2 evolution rate in the alkaline medium was significantly higher than that in the acidic medium during the change of the pH value of the solution from 3 to 14, and the H_2 evolution rate reached the maximum at pH 13.
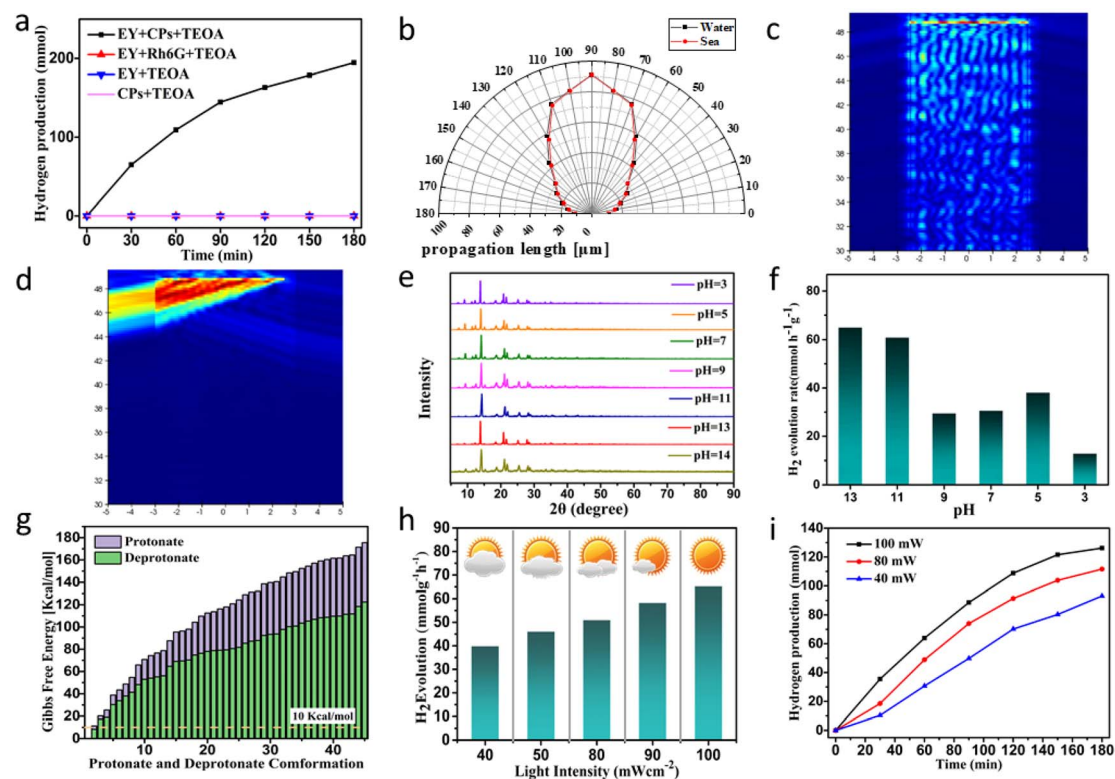
Fig. 4 Photocatalytic performance. (a) Time-dependent photocatalytic hydrogen production on the EY-sensitized Pd/Pd(II)CP system, EY-sensitized Rh6G system, and only Pd/Pd(II)CPs (500 mW cm^{-2}). (b) The propagation length of light in the microtube when the light source is incident at different angles. The electric field intensity distribution in the microtube at normal incidence (c) and a small angle. (d) Powder XRD patterns of Pd/Pd(II)CPs soaked in acidic or basic solutions for 24 h. (e) Photocatalytic activity under acidic and alkaline conditions (100 mW cm^{-2}). (f) The protonation and deprotonation reactions of the 45 lowest energy conformations and Gibbs free energy by elliptic potential test solution. (g) Photocatalytic activity under various light intensities. (h) Photocatalytic activity in seawater under visible light irradiation with different power densities. (i) Photocatalytic activity in seawater under visible light irradiation with different power densities.

To explain the high stability of the Pd/Pd(II)CPs in a broad pH range from 3 to 14 and the high hydrogen evolution rate under the alkaline reaction conditions, we calculate 45 low-energy protonated and deprotonated conformations through an ellipsoidal potential, see Movies 1 and 2.† The Gibbs free energies of the protonation and deprotonation processes are calculated. Fig. 4g shows that all the energies are greater than 10 kcal mol^{-1}, which indicates that neither protonation nor deprotonation can occur easily at room temperature. On the other hand, for each conformation, the protonation energy is lower than the deprotonation energy, which explains why alkaline conditions' catalytic effect is better than that of acidic conditions.

To make the photocatalysts be used in practical applications, the photocatalytic system needs to maintain high catalytic activity even at low light power because global solar radiation varies with the location, weather, and other conditions. In addition, solar radiation power is usually less than 100 mW cm^{-2}.[42] To examine the adaptable catalytic ability of Pd/Pd(II) CPs, a photocatalytic experiment was performed by gradually increasing the intensity of the irradiation light. Here, the light intensity is set to 40, 50, 80, 90 and 100 mW cm^{-2} from low to high, respectively. As shown in Fig. 4h, the catalyst could reach

a hydrogen production rate of 39.9 mmol h^{-1} g^{-1} under light power (40 mW cm^{-2}) close to morning sunlight or cloudy sky, indicating the superior practicability of this photocatalytic system. In addition, the photocatalytic activity of Pd/Pd(II)CPs in seawater was also evaluated. Fig. S14† shows that the formed Pd/Pd(II)CPs displayed high stability in seawater. As shown in Fig. 4i, the hydrogen production rates of 37.8 mmol h^{-1} g^{-1}, 48.9 mmol h^{-1} g^{-1}, and 63.9 mmol h^{-1} g^{-1} were obtained at an irradiation light intensity of 40 mW cm^{-2}, 80 mW cm^{-2}, and 100 mW cm^{-2} in seawater, respectively.

Pd/Pd(II)CPs exhibited high apparent quantum efficiency (AQE) under the irradiation of different monochromatic light intensities in the absorption range, and the highest AQE could reach 50% at 500 nm (Fig. S15†) due to the absorption of H- and J-type[43] aggregates in concentrated solution or semiconductor surfaces.[44] Besides their great hydrogen evolution activity, Pd/Pd(II)CPs also demonstrated impressive photostability. As shown in Fig. S16,† recycling experiments indicated that only a slight decay in activity was observed during the five photocatalytic runs. The tubular structure of the Pd/Pd(II)CPs is basically maintained after the five cycles (Fig. S17a†). The TEM image (Fig. S17b†) shows that the inside of the material still has a hollow tubular morphology with good stability. The number of

Pd nanoparticles distributed on the catalyst surface increased significantly, because Pd ions in the material were reduced to Pd nanoparticles by partial photoelectrons with the progress of the catalytic reaction. Moreover, the PXRD patterns of Pd/Pd(II)CPs evidenced good maintenance of the crystallinity after five successive runs for H_2 production (Fig. S18†), indicating the excellent stability of the present H_2 production system.

To gain insight into the high H_2 production performance of Pd/Pd(II)CPs and explore their internal electron transfer dynamics, the internal resistance of the sample charge transfer process was evaluated by the electrochemical impedance spectroscopy (EIS) measurement method. The Nyquist curve shows that the EY-sensitized Pd/Pd(II)CP system presented a smaller semicircular diameter compared to Pd/Pd(II)CPs and Pd/Pd(II)CPRs (Fig. 5a), indicating that the Pd/Pd(II)CP system had a smaller interface charge transfer resistance. The transient photocurrent responses showed that the charge transfer from the EY excited state to the Pd/Pd(II)CPs was significantly improved compared to the Pd/Pd(II)CPs alone (Fig. 5b), indicating that both the charge separation efficiency and charge carrier migration rates were significantly improved.

To further investigate the charge separation capability, a fluorescence titration experiment was carried out. Fig. S19† shows that the aqueous solution of EY emits strong fluorescence emission at 537 nm due to the recombination of the excited charge pairs. When Pd/Pd(II)CPs and Pd/Pd(II)CPRs were introduced, the peak intensity of the EY emission was significantly reduced. At the same time, the emission peak appeared slightly red-shifted (Fig. 5c). This shift is mainly attributed to the π–π interaction between Rh6G and EY attached to Pd/Pd(II)CPs,[38] which facilitates the transfer of electrons from photoexcited EY to Pd/Pd(II)CPs. Fitting of the curves showed that the fluorescence lifetimes (t) of EY and EY-sensitized Pd/Pd(II)CPs were 0.732 ns and 0.506 ns, respectively (Fig. 5d). The obvious fluorescence quenching and lifetime diminution indicated the effective charge transfer from EY to Pd/Pd(II)CPs, further confirming the excellent charge separation and migration capabilities of this photocatalyst system.

Fig. 5e shows the proposed mechanism of the EY-sensitized Pd/Pd(II)CP photocatalytic system. There is electron transfer between the catalyst and the photosensitizer, which is confirmed by photocurrent response (Fig. 5b) and PL spectra (Fig. S19†). Under visible light irradiation, EY molecules adsorbed on the surface of Pd/Pd(II)CPs are excited from the highest occupied molecular orbital (HOMO) to the lowest unoccupied molecular orbital (LUMO) state, which is confirmed by PL spectra (Fig. S19†). This excited electron transfers to Pd(II) CPs and then to the surface of the loaded Pd nanoparticles where the protons are reduced to form molecular H_2.[44–49] In addition, the content of EY adsorbed on the catalyst also has
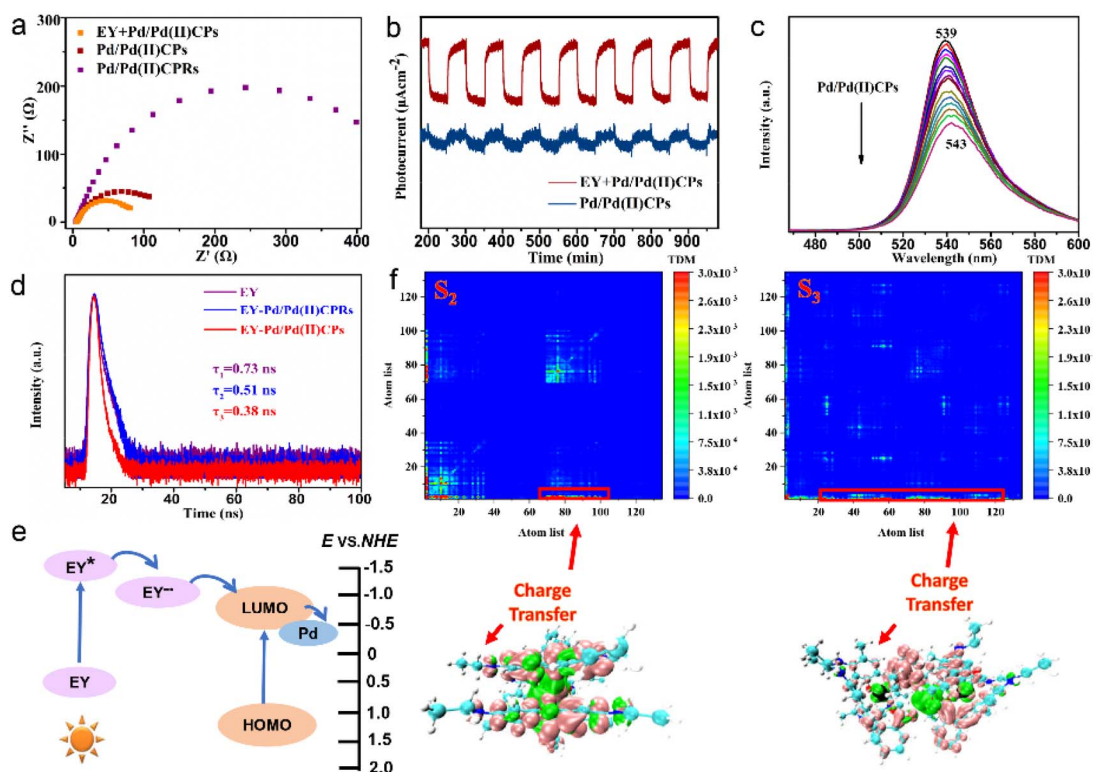
Fig. 5 (a) Electrochemical impedance spectroscopy Nyquist plots. (b) Photocurrent responses. (c) Steady-state PL emission spectra ($\lambda_{ex} = 380$ nm). (d) Time-resolved PL spectra of Pd/Pd(II)CPs and Pd/Pd(II)CPRs. (e) Mechanism schematic of the facilitated charge-carrier separation through the EY-sensitized Pd/Pd(II)CP system. (f) The excited state transition electron density matrix and electron−hole pair density isosurface (green and pink isosurfaces represent the electron and hole densities, respectively) of S_2 and S_3 for the Pd/Pd(II)CP structure searched by MTD-GC.

a significant impact on the catalytic activity of hydrogen evolution. From Fig. S20,† it can be seen that the activity increases with the increase of EY and then gradually decreases. This is because free dye molecules in the solution cannot participate in electron transfer. In addition, in the absence of EY, there is no H_2 detected (Fig. 4a), indicating that the EY is the only important electron donor in the system. Moreover, the EIS, photocurrent responses, steady-state PL emission spectra, and time-resolved PL spectra confirmed the better charge transfer in the EY-sensitized Pd/Pd(ɪɪ)CP system photocatalyst compared with its independent counterparts.

To further illustrate the above electron transfer process, excited-state calculations are performed using the time-dependent density functional theory method combined with the CAM-B3LYP7 general function and def2-TZVP basis set. Based on the Pd(ɪɪ)CP structure searched by MTD-GC, the theoretical absorption spectrum of Pd(ɪɪ)CPS was calculated by the TDDFT method. As shown in Fig. S21,† we selected two characteristic excited states S_2 and S_3 of the absorption peak which associated with the luminescent region of EY for electron–hole pair analysis. Fig. 5f shows that there is a photo-induced charge transfer from rhodamine 6G to Pd atoms after the rhodamine 6G molecules receive photo-excitation in the current region, and the electrons will enhance the catalytic effect of Pd.

4. Conclusions

In summary, novel rhodamine-based coordination polymer hollow tubes embedded with Pd NPs were successfully synthesized via a facile photochemical method for photocatalytic H_2 evolution in a wide pH range and seawater. The FDTD algorithm showed that the formation of a 1D hollow structure has a good confinement effect on light, so more light is involved in the catalytic reaction. As a result, the resulting Pd/Pd(ɪɪ)CP super-structures exhibited excellent photocatalytic H_2 evolution activity under visible light irradiation, and its hydrogen evolution rate was 112.3 mmol h^{-1} g^{-1}, which was much higher than that of reported CP-based photocatalysts reported so far. More importantly, due to the high Gibbs free energies of protonation and deprotonation, such a photocatalytic system exhibits high stability and efficient photocatalytic H_2 evolution in a wide pH range and seawater under visible light close to morning or cloudy sunlight. The design strategy of this study opens up a new pathway to construct high-performance CP-based pho-tocatalysts with wide pH catalytic activity for highly efficient solar-to-fuel energy conversion in practical applications.

Conflicts of interest

There are no conflicts to declare.

Acknowledgements

References

1 M. D. Karkas, O. Verho, E. V. Johnston and B. Akermark, *Chem. Rev.*, 2014, **114**, 11863–12001.

2 H. Wang, L. Zhang, Z. Chen, J. Hu, S. Li, Z. Wang, J. Liu and X. Wang, *Chem. Soc. Rev.*, 2014, **43**, 5234–5244.

3 Q. Wang and K. Domen, *Chem. Rev.*, 2020, **120**, 919–985.

4 A. Fujishima and K. Honda, *Nature*, 1972, **238**, 37–38.

5 S. Zhu and D. Wang, *Adv. Energy Mater.*, 2017, **7**, 1700841.

6 Y. Ma, X. Wang, Y. Jia, X. Chen, H. Han and C. Li, *Chem. Rev*, 2014, **114**, 9987–10043.

7 S. Wu, J. M. L. Madridejos, J. K. Lee, Y. Lu, R. Xu and Z. Zhang, *Nanoscale*, 2023, **15**, 3449–3460.

8 M. Zhang, X. Chen, X. Jiang, J. Wang, L. Xu, J. Qiu, W. Lu, D. Chen and Z. Li, *ACS Appl. Mater. Interfaces*, 2021, **13**, 14198–14206.

9 M. Tan, C. Yu, H. Zeng, C. Liu, W. Dong, H. Meng, Y. Su, L. Qiao, L. Gao, Q. Lu and Y. Bai, *Nanoscale*, 2023, **15**, 2425–2434.

10 C. Bie, L. Wang and J. Yu, *Chem*, 2022, **8**, 1567–1574.

11 M. A. Green and S. P. Bremner, *Nat. Mater.*, 2016, **16**, 23–34.

12 L. Li, Z. Zhou, L. Li, Z. Zhuang, J. Bi, J. Chen, Y. Yu and J. Yu, *ACS Sustainable Chem. Eng.*, 2019, **7**, 18574–18581.

13 L. Feng, K. Y. Wang, T. H. Yan and H. C. Zhou, *Chem. Sci.*, 2020, **11**, 1643–1648.

14 Y. He, W. Zhou, G. Qian and B. Chen, *Chem. Soc. Rev.*, 2014, **43**, 5657–5678.

15 N. Poldme, L. O'Reilly, I. Fletcher, J. Portoles, I. V. Sazanovich, M. Towrie, C. Long, J. G. Vos, M. T. Pryce and E. A. Gibson, *Chem. Sci.*, 2019, **10**, 99–112.

16 G. Li, M. F. Mark, H. Lv, D. W. McCamant and R. Eisenberg, *J. Am. Chem. Soc.*, 2018, **140**, 2575–2586.

17 D. E. Williams, J. A. Rietman, J. M. Maier, R. Tan, A. B. Greytak, M. D. Smith, J. A. Krause and N. B. Shustova, *J. Am. Chem. Soc.*, 2014, **136**, 11886–11889.

18 S. Wang, B. Y. Guan and X. W. D. Lou, *J. Am. Chem. Soc.*, 2018, **140**, 5037–5040.

19 B. Qiu, Q. Zhu, M. Du, L. Fan, M. Xing and J. Zhang, *Angew. Chem., Int. Ed.*, 2017, **56**, 2684–2688.

20 J. Chen, J. Chen and Y. Li, *J. Mater. Chem. A*, 2017, **5**, 24116–24125.

21 D. Zheng, X. N. Cao and X. Wang, *Angew. Chem., Int. Ed.*, 2016, **55**, 11512–11516.

22 N. Wang, G. Cheng, L. Guo, B. Tan and S. Jin, *Adv. Funct. Mater.*, 2019, **29**, 1904781.

23 Y. Wang, X. Liu, J. Liu, B. Han, X. Hu, F. Yang, Z. Xu, Y. Li, S. Jia, Z. Li and Y. Zhao, *Angew. Chem., Int. Ed.*, 2018, **57**, 5765–5771.

24 Y. Liu, L. Wang, H. Feng, X. Ren, J. Ji, F. Bai and H. Fan, *Nano Lett.*, 2019, **19**, 2614–2619.

25 T. Oshima, S. Nishioka, Y. Kikuchi, S. Hirai, K. I. Yanagisawa, M. Eguchi, Y. Miseki, T. Yokoi, T. Yui,

K. Kimoto, K. Sayama, O. Ishitani, T. E. Mallouk and K. Maeda, *J. Am. Chem. Soc.*, 2020, **142**, 8412–8420.

26 S. E. Lee, A. Nasirian, Y. E. Kim, P. T. Fard, Y. Kim, B. Jeong, S. J. Kim, J. O. Baeg and J. Kim, *J. Am. Chem. Soc.*, 2020, **142**, 19142–19149.

27 S. S. Ramos, A. F. Vilhena, L. Santos and P. Almeida, *Magn. Reson. Chem.*, 2000, **38**, 475–478.

28 L. Andrews and A. Citra, *Chem. Rev*, 2002, **102**, 885–912.

29 L. Fan and T. Ziegler, *J. Phys. Chem.*, 1992, **96**, 6937–6941.

30 Q. Sun, N. Wang, J. Yu and J. C. Yu, *Adv. Mater.*, 2018, **30**, e1804368.

31 L. Li, X. Chen, Y. Wu, D. Wang, Q. Peng, G. Zhou and Y. Li, *Angew. Chem., Int. Ed.*, 2013, **52**, 11049–11053.

32 M. C. di Gregorio, P. Ranjan, L. Houben, L. J. W. Shimon, K. Rechav, M. Lahav and M. E. van der Boom, *J. Am. Chem. Soc.*, 2018, **140**, 9132–9139.

33 Y. Xia, Y. Xiong, B. Lim and S. E. Skrabalak, *Angew. Chem., Int. Ed.*, 2009, **48**, 60–103.

34 H. Cheng, N. Yang, G. Liu, Y. Ge, J. Huang, Q. Yun, Y. Du, C. J. Sun, B. Chen, J. Liu and H. Zhang, *Adv. Mater.*, 2020, **32**, e1902964.

35 D. Sheberla, L. Sun, M. A. Blood-Forsythe, S. Er, C. R. Wade, C. K. Brozek, A. Aspuru-Guzik and M. Dinca, *J. Am. Chem. Soc.*, 2014, **136**, 8859–8862.

36 W. Huang, Q. He, Y. Hu and Y. Li, *Angew. Chem., Int. Ed.*, 2019, **58**, 8676–8680.

37 Y. Huang, Y. Fang, X. F. Lu, D. Luan and X. W. Lou, *Angew. Chem., Int. Ed.*, 2020, **59**, 19914–19918.

38 S. Wang, B. Y. Guan, X. Wang and X. W. D. Lou, *J. Am. Chem. Soc.*, 2018, **140**, 15145–15148.

39 X. Y. Dong, M. Zhang, R. B. Pei, Q. Wang, D. H. Wei, S. Q. Zang, Y. T. Fan and T. C. Mak, *Angew. Chem., Int. Ed.*, 2016, **55**, 2073–2077.

40 J. Xu, Y. Qi and L. Wang, *Appl. Catal., B*, 2019, **246**, 72–81.

41 F. Leng, H. Liu, M. Ding, Q.-P. Lin and H.-L. Jiang, *ACS Catal.*, 2018, **8**, 4583–4590.

42 X. Yang, Z. Hu, Q. Yin, C. Shu, X. F. Jiang, J. Zhang, X. Wang, J. X. Jiang, F. Huang and Y. Cao, *Adv. Funct. Mater.*, 2019, **29**, 1808156.

43 S. Min and G. Lu, *J. Phys. Chem. C*, 2012, **116**, 19644–19652.

44 W. Zhen, H. Gao, B. Tian, J. Ma and G. Lu, *ACS Appl. Mater. Interfaces*, 2016, **8**, 10808–10819.

45 K.-Q. Lu, L. Yuan, X. Xin and Y.-J. Xu, *Appl. Catal., B*, 2018, **226**, 16–22.

46 J. Willkomm, K. L. Orchard, A. Reynal, E. Pastor, J. R. Durrant and E. Reisner, *Chem. Soc. Rev.*, 2016, **45**, 9–23.

47 W. Zhen, J. Ma and G. Lu, *Appl. Catal., B*, 2016, **190**, 12–25.

48 S. H. Li, N. Zhang, X. Xie, R. Luque and Y. J. Xu, *Angew. Chem., Int. Ed.*, 2018, **57**, 13082–13085.

49 X. Meng, Y. Dong, Q. Hu and Y. Ding, *ACS Sustainable Chem. Eng.*, 2018, **7**, 1753–1759.